OPEN ACCESS Freely available online



# Using Structural Information to Change the Phosphotransfer Specificity of a Two-Component Chemotaxis Signalling Complex

**Christian H. Bell[1,2☯], Steven L. Porter[1☯¤], Annabel Strawson[1], David I. Stuart[2]*, Judith P. Armitage[1]***

**1** Oxford Centre for Integrative Systems Biology, Department of Biochemistry, University of Oxford, Oxford, United Kingdom, **2** Division of Structural Biology, University of Oxford, Oxford, United Kingdom

## Abstract

Two-component signal transduction pathways comprising histidine protein kinases (HPKs) and their response regulators (RRs) are widely used to control bacterial responses to environmental challenges. Some bacteria have over 150 different two-component pathways, and the specificity of the phosphotransfer reactions within these systems is tightly controlled to prevent unwanted crosstalk. One of the best understood two-component signalling pathways is the chemotaxis pathway. Here, we present the 1.40 Å crystal structure of the histidine-containing phosphotransfer domain of the chemotaxis HPK, $CheA_3$, in complex with its cognate RR, $CheY_6$. A methionine finger on $CheY_6$ that nestles in a hydrophobic pocket in $CheA_3$ was shown to be important for the interaction and was found to only occur in the cognate RRs of $CheA_3$, $CheY_6$, and $CheB_2$. Site-directed mutagenesis of this methionine in combination with two adjacent residues abolished binding, as shown by surface plasmon resonance studies, and phosphotransfer from $CheA_3$-P to $CheY_6$. Introduction of this methionine and an adjacent alanine residue into a range of noncognate CheYs, dramatically changed their specificity, allowing protein interaction and rapid phosphotransfer from $CheA_3$-P. The structure presented here has allowed us to identify specificity determinants for the CheA–CheY interaction and subsequently to successfully reengineer phosphotransfer signalling. In summary, our results provide valuable insight into how cells mediate specificity in one of the most abundant signalling pathways in biology, two-component signal transduction.

**Citation:** Bell CH, Porter SL, Strawson A, Stuart DI, Armitage JP (2010) Using Structural Information to Change the Phosphotransfer Specificity of a Two-Component Chemotaxis Signalling Complex. PLoS Biol 8(2): e1000306. doi:10.1371/journal.pbio.1000306

**Academic Editor:** Gregory A. Petsko, Brandeis University, United States of America

**Received** October 12, 2009; **Accepted** December 31, 2009; **Published** February 9, 2010



**Funding:** This study was funded by the Wellcome Trust and the BBSRC (Biotechnology and Biological Sciences Research Council). The funders had no role in study design, data collection and analysis, decision to publish, or preparation of the manuscript.

**Competing Interests:** The authors have declared that no competing interests exist.

**Abbreviations:** RR, response regulator; SPR, surface plasmon resonance

* E-mail: dave@strubi.ox.ac.uk (DIS); judith.armitage@bioch.ox.ac.uk (JPA)

☯ These authors contributed equally to this work.

¤ Current address: School of Biosciences, University of Exeter, Exeter, United Kingdom

## Introduction

Bacteria, Archaea, and some eukaryotes use two-component signalling pathways to detect environmental conditions and bring about appropriate changes in cellular behaviour [1,2]. Two-component pathways comprise sensor histidine kinases (HPK) and response regulators (RRs). Environmental stimuli control the rate at which the HPK autophosphorylates on a conserved histidine residue. Once phosphorylated, the HPK transfers the phosphoryl group to an aspartate residue within the receiver domain of the cognate RR. The phosphorylated RR (RR-P), often a transcriptional regulator, then effects a response appropriate to the original stimulus. Some bacteria have over 150 different HPK and RR pairs, and the specificity of the phosphorylation reactions between them needs to be tightly controlled to prevent HPKs from inappropriately phosphorylating and activating noncognate RRs. A number of mechanisms contribute to this specificity [3,4], although the primary one is molecular recognition, in which a HPK shows a strong kinetic preference for its cognate RRs [5,6]. Understanding the mechanisms involved in molecular recognition will not only allow prediction of interacting pairs, but potentially allow the rewiring of bacterial sensory pathways for use in synthetic biology.

Many two-component systems utilize an additional element, the Hpt (histidine-containing phosphotransfer) domain in phosphotransfer; these include multistep phosphorelays and chemotaxis signalling pathways. In multistep phosphorelays, the Hpt domain serves as an intermediate in the transfer of phosphoryl groups from the receiver domain phosphorylated by the HPK and the output RR. In contrast, the histidine within the Hpt domain is the initial site of phosphorylation in the chemotaxis HPK, CheA, and is phosphorylated using ATP as the phosphodonor [7]. Subsequently, the phosphoryl group is transferred from the histidine residue in the Hpt (P1) domain of CheA to an aspartate residue on either of two RRs, CheY or CheB [8]. In this study, we present the structure of the Hpt (P1) domain of $CheA_3$ from *R. sphaeroides* in complex with its cognate RR $CheY_6$, which, to our knowledge, is the first structure of a Hpt domain of a CheA protein in complex with its RR.

## Author Summary

The ability to respond to environmental stimuli is a universal feature of living cells. Evolution has created a vast array of signalling mechanisms that enable cells to react in many ways to extracellular changes. In bacteria, two-component signalling mechanisms, comprising a sensor protein kinase paired with its a cognate response regulator, are used widely to sense and respond to environmental changes. Some species of bacteria have over 150 different two-component pairs in a single cell, so the specificity between these pairs has to be tightly controlled to prevent "crossed wires" between signalling pathways. In this study, we have identified the determinants of this specificity in a two-component complex that controls the movement of *Rhodobacter sphaeroides* along a chemical gradient. By solving and analysing the crystal structure of this complex, we were able to pinpoint the amino acid residues that are crucially involved in formation of the complex. Knowledge of these crucial residues allowed us to convert noncognate response regulators into cognate response regulators simply by changing two amino acids. This reengineering of two-component signalling pathways paves the way for producing custom-designed circuits for applications in synthetic biology.


The chemotaxis pathway of *Escherichia coli* has been extensively characterized [9–12]. However, many bacteria have more complicated chemosensory pathways, employing multiple homologues of each of the chemosensory proteins [13–15]. *R. sphaeroides* has four CheA homologues and eight chemotaxis RR proteins (six CheYs and two CheBs) plus multiple homologues of the other *E. coli* chemotaxis proteins [13,16–18]. Interestingly, the different CheAs show different phosphotransfer specificities for the CheY and CheB homologues [19–22]. $CheA_3$ and $CheA_4$ form a cluster with the soluble chemoreceptors in the cytoplasm, which is believed to sense the metabolic state of the cell [13,23,24]. $CheA_3$ and $CheA_4$ are unusual CheAs that lack some of the domains found in *E. coli* CheA [20,25]. $CheA_4$ has a P3 (dimerization) domain, a P4 (kinase) domain, and a P5 (regulatory) domain, whereas $CheA_3$ has a P1 (Hpt) domain and a P5 (regulatory) domain separated by a 794-amino acid sequence that encodes a novel CheY-P phosphatase activity [26]. Neither $CheA_3$ nor $CheA_4$ is capable of autophosphorylation; instead, $CheA_4$ phosphorylates $CheA_3$ on H51 of the P1 (Hpt) domain. Once phosphorylated, $CheA_3$-P serves as a specific phosphodonor for the chemotaxis RRs, $CheY_1$, $CheY_6$, and $CheB_2$. However, it is unable to phosphorylate the other chemotaxis RRs, $CheY_2$, $CheY_3$, $CheY_4$, $CheY_5$, and $CheB_1$ [20,21,27]. This phosphotransfer specificity must be determined by the interactions between the RRs and the P1 domain of $CheA_3$ since the isolated P1 domain of $CheA_3$ ($CheA_3P1$) shows the same phosphotransfer specificity as full-length $CheA_3$ [26].

In groundbreaking work, the Laub group used a mutual information bioinformatics approach to identify coevolving residues in HPKs and their cognate RRs [28]. They reasoned that many of the coevolving residues would be the specificity determinants for the phosphotransfer reaction and went on to show that it is possible to switch the RR substrate specificity of the HPK EnvZ by mutating these residues [28]. In this study, we use a structure-based approach to identify specificity determinants for the phosphotransfer reaction between $CheA_3P1$-P and $CheY_6$. By introducing these residues into the noncognate RRs, we have been able to change their kinase specificity, allowing them to be phosphorylated by $CheA_3P1$-P.

## Results

### Structure of the $CheA_3P1.CheY_6$ Complex

In order to elucidate the molecular details of the interaction between $CheA_3$ and $CheY_6$, the complex structure of $CheY_6$ and the unphosphorylated Hpt domain of $CheA_3$ (residues 1–135) has been solved to 1.40 Å using Seleno single-wavelength anomalous dispersion (SAD) for phasing. Data collection and refinement statistics can be found in Table 1.

$CheY_6$ has the typical $(\alpha/\beta)_5$ topology seen for *E. coli* CheY [29] and other structurally characterized RRs (Figure 1). Comparison with *E. coli* CheY reveals a high degree of structural conservation with a root mean square deviation (rmsd) of 1.4 Å over 115 Cα atoms (26% sequence identity). Although crystallized in the presence of $Mn^{2+}$, there was no additional density in the $CheY_6$ divalent cation binding site. However, the conformation of the metal coordinating residues Asp56, Asp9, and Asp10 is most similar to that found in the structure of $Mg^{2+}$ bound CheY [30]. Only the backbone carbonyl of Glu58 is facing away rather than pointing towards the potential metal binding site (Figure S1). $CheY_6$ has an elongated loop region connecting β5 and α5 (Figure 1). This loop comprises 13 residues (residues 107–119) in $CheY_6$ compared to only three residues (109–111) in *E. coli* CheY. In the crystal, this loop is only partially ordered, suggesting that it is highly flexible. Residues 113–118 could not be traced and were omitted from the final model. The N-terminal region of this β5-α5 loop in combination with α1 of $CheY_6$ form the vast majority of contacts to $CheA_3P1$ (Figure 1).

$CheA_3P1$ forms a four-helix bundle (αA–αD) with an additional C-terminal helix (αE) (Figure 1). Despite low sequence identity, it is structurally very similar to previously determined CheA P1 structures [31–33]. Comparison with CheA P1 from *Salmonella enterica* serovar Typhimurium [32] and *Thermotoga maritima* [33] gives an rmsd of 1.2 Å over 116 Cα atoms (21% sequence identity) and 1.5 Å over 101 Cα (18% sequence identity), respectively. The site of phosphorylation, His51 in $CheA_3P1$, is located on αB, in close proximity to the active site of the RR (Figure 1) with the phosphoacceptor Asp56 on $CheY_6$ being 7.5Å from His51 on $CheA_3P1$. Helices αA and αB face the RR and together with the αB–αC loop form the interface with $CheY_6$ (Figure 1).

### Structure of Phosphorylated $CheA_3P1$ in Complex with $CheY_6$(D56N, S83A)

To show that the conclusions drawn from the unphosphorylated structure are also valid for the physiologically relevant, phosphorylated complex, we solved the structure of phosphorylated $CheA_3P1$ in complex with $CheY_6$. Since the rapid rate of phosphotransfer between $CheA_3P1$-P and $CheY_6$ does not allow crystallization of the wild-type, phosphorylated complex, we formed a stable, complex by introducing two substitutions, D56N and S83A, in the active site of $CheY_6$ (see Materials and Methods for details). These substitutions have previously been shown to abolish phosphotransfer from $CheA_3P1$-P [19]. The structure was solved to 2.8 Å by molecular replacement using the unphosphorylated structure as model. Data collection and refinement statistics can be found in Table 1. The structure shows clear additional density adjacent to Nε2 of His51 of $CheA_3P1$ in agreement with phosphorylation of this residue (Figure S2). Due to the moderate resolution of the analysis, residues 60–65, 85–97, and 111–121 on $CheY_6$ could not be traced and were not included in the final model.

**Table 1.** Data collection and refinement statistics.

| Data Collection and Refinement | Statistics | Subcategory | SeMet | Unphosphorylated | Phosphorylated |
|---|---|---|---|---|---|
| **Data collection** | Resolution (Å) | | 2.3 (2.38–2.30)[a] | 1.40 (1.45–1.40) | 2.80 (2.90–2.80) |
| | Space group | | $P2_1$ | $P2_1$ | P1 |
| | Cell dimension | *a*, *b*, *c* (Å) | 43.8, 62.7, 49.1 | 43.7, 62.0, 48.9 | 33.2, 43.4, 48.7 |
| | | α, β, γ (°) | 90, 101.1, 90 | 90, 101.3, 90 | 78.8, 86.6, 80.9 |
| | Redundancy | | 9.5 (10.1) | 6.3 (3.7) | 1.8 (1.8) |
| | Completeness (%) | | 99.2 (99.0) | 99.7 (98.9) | 96.1 (94.5) |
| | Rsym (%) | | 8.9 (19.7) | 5.3 (14.8) | 12.0 (61.6) |
| | Avg I/σ | | 18.4 (12.9) | 31.6 (9.8) | 6.3 (1.2) |
| **Refinement** | Resolution | | | 38–1.40 | 42–2.80 |
| | No. reflections | | | 50287 | 6232 |
| | $R_{work}/R_{free}$ | | | 17.0/20.7 | 24.1[b]/28.4[b] |
| | No. atoms | Protein | | 2040 | 1743 |
| | | Water | | 272 | — |
| | B-factors (Å$^2$) | Protein | | 28.5 | 86.5[c] |
| | | Water | | 38.9 | — |
| | r.m.s. deviations | Bond lengths (Å) | | 0.010 | 0.008 |
| | | Bond angles (°) | | 1.220 | 0.950 |

[a]Numbers in parenthesis are for the highest resolution shell.
[b]Rxpct, as described elsewhere [43].
[c]Standard deviation of ±18 Å$^2$.
doi:10.1371/journal.pbio.1000306.t001

Compared to the unphosphorylated complex, $CheA_3P1$-P undergoes a rigid body translation of 2.1 Å relative to the RR (Figure 2A). This realignment of $CheA_3P1$-P positions the phosphorylated His51 closer to the phosphoacceptor on $CheY_6$, Asp56 (Figure 2B). The phosphorylated His51 is facing away from the active site of $CheY_6$; however, a 180° flip of this side chain would put it in near linear geometry and place the phosphoryl group within 4.5 Å of Asp56 of $CheY_6$ (Figure 2B). The orientation of the phosphorylated His51 seen in the crystal structure is likely caused by the lack of a divalent cation in the metal binding site of the RR leading to electrostatic repulsion from the $CheY_6$ active site.

The difference in binding affinity for $CheY_6$ between $CheA_3$ and $CheA_3$-P is not known. In *E. coli*, the difference in $K_d$ values for CheY between CheA and CheA-P is relatively small, with both values being in the low micromolar range [34]. Consistent with this, we find very little change in the total buried surface area between the phosphorylated (605 Å$^2$) and unphosphorylated (530 Å$^2$) structures of $CheA_3P1$ complexed with $CheY_6$. The only difference is a hydrogen bond formed between Glu58 of $CheY_6$ and His51 of $CheA_3P1$ in the unphosphorylated complex that is released in the phosphorylated complex. As this is not contributing to the interface of the physiologically important complex, it is therefore not

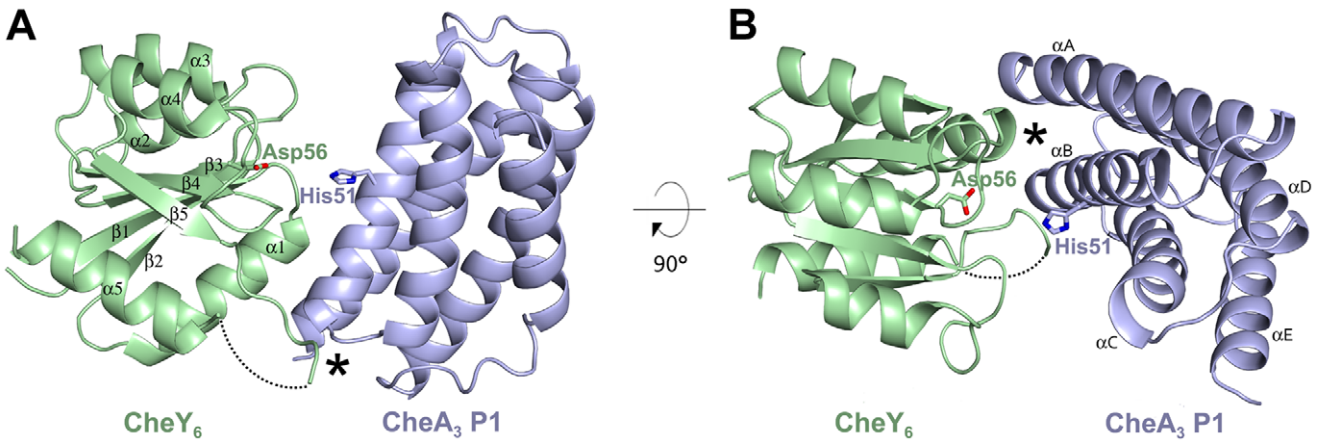


**Figure 1. Structure of the $CheA_3P1.CheY_6$ complex.** $CheA_3P1$ is shown in light blue whereas $CheY_6$ is in pale green. The phosphorylatable residue of $CheA_3P1$, His51, and the phosphoacceptor on $CheY_6$, Asp56, are shown in stick representation. Secondary structure elements are labelled in black. Residues 113–118 of $CheY_6$ could not be traced and are depicted as a dotted line. (A) Side view onto the $CheA_3P1.CheY_6$ complex with the interaction between β5 and α5 in $CheY_6$ and αB, and the following loop connecting αB and αC on $CheA_3P1$, marked with an asterisk. (B) Top view showing the major site of interaction between the N-terminal end of α1 on $CheY_6$ and αA/αB on $CheA_3P1$ marked by an asterisk.
doi:10.1371/journal.pbio.1000306.g001

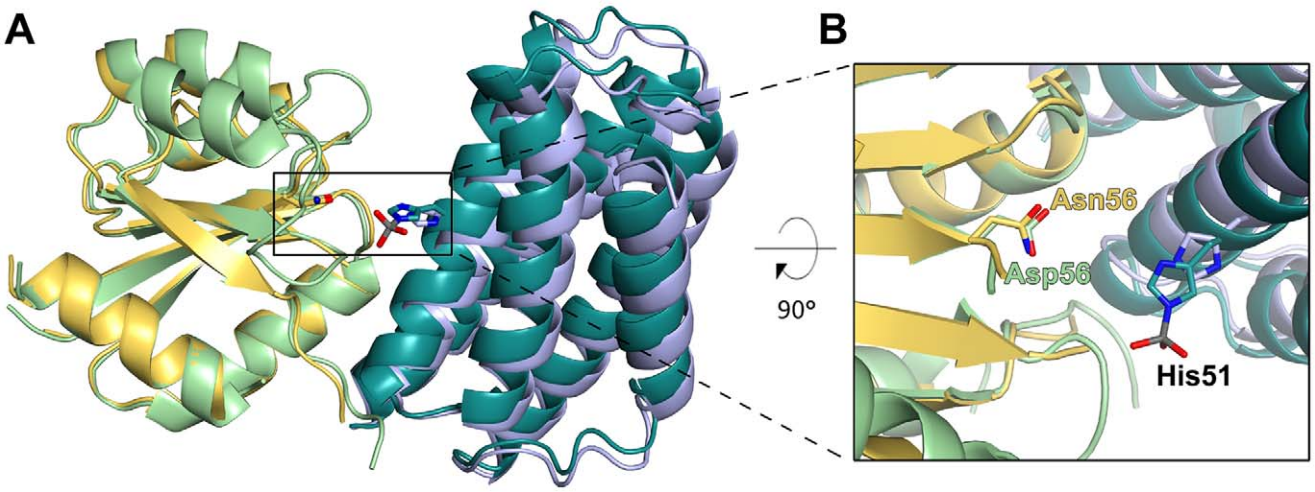


**Figure 2. Superposition of the $CheA_3P1.CheY_6$ complex in the phosphorylated and unphosphorylated conformations.** Structures were aligned onto the RR. Colour coding for the unphosphorylated conformation as in Figure 1; for the phosphorylated conformation, $CheY_6$ is shown in yellow and $CheA_3$ P1 in teal. The active site residues His51 ($CheA_3$ P1) and Asp56/Asn56 ($CheY_6$ unphosphorylated/phosphorylated complex conformation) are shown in stick representation. (A) Overview highlighting the 2.1 Å rigid body translation of $CheA_3$ P1 towards $CheY_6$. (B) Close-up view onto the active site showing the movement of His51 towards Asp56/Asn56.
doi:10.1371/journal.pbio.1000306.g002

discussed further. Because the interfaces in the phosphorylated and unphosphorylated complex are highly similar, the following discussion of the interactions between $CheA_3P1$ and $CheY_6$ are based on the high-resolution, unphosphorylated structure.

## Interactions between $CheA_3P1$ and $CheY_6$

The interface between $CheA_3P1$ and $CheY_6$ is dominated by hydrophobic interactions with only one hydrogen bond and no salt bridges formed between the two proteins. The buried surface area of the interface is small (530 $Å^2$), indicative of a weak interaction, consistent with the transient nature of the complexes [35]. A continuous interface is formed by two sites of interaction complemented by a hydrogen bond formed between Ser83 on $CheY_6$ and Arg58 on $CheA_3P1$. One of these sites lies between the elongated loop region between β5 and α5 in $CheY_6$ and αB and the following loop connecting αB and αC on $CheA_3P1$ (Figure 1A). The other site lies between the N-terminal end of α1 on $CheY_6$ and αA/αB on $CheA_3P1$ (Figure 1B). The latter is the major binding site including ~70% of the total buried surface area (358 $Å^2$).

In this region, helices αA and αB of $CheA_3P1$ form a hydrophobic pocket comprising Ile11, Leu14, and Tyr15 on αA, and Asn56, Val59, and Leu60 on αB (Figure 3A and 3B). This pocket is situated adjacent to α1 on $CheY_6$ and in ideal position to accommodate Met13 on the N-terminal region of this helix. This Met finger is protruding from α1, and its side chain fits snugly into the hydrophobic pocket, with 99.7% of its accessible surface area being buried (Figure 3B). The hydrophobic interaction is complemented by Ala12, Leu16, and Tyr17 of α1 on $CheY_6$, all facing the same side on $CheA_3P1$ as Met13 (Figure 3A). Ala12 of $CheY_6$ extends the hydrophobic interface by interaction with Leu14 of $CheA_3P1$, whereas Leu16 of $CheY_6$ interacts with Ile11 and the aliphatic part of Glu10 on αA of $CheA_3P1$. Tyr17 extends the binding surface towards the β5-α5 loop by interacting with Val59 at the C-terminus of αB. The elongated loop between β5 and α5 of $CheY_6$ forms van der Waals interactions with Ser109, Gly110, and Thr111 of $CheY_6$ contacting Ile59, Gly61, and Ser63 on αB and the following loop region on $CheA_3P1$ (Figure 3C). A main chain hydrogen bond is formed between Gly110 and Val59.

Of these interactions, the Met13 finger has the largest contribution towards the binding interface on $CheY_6$, accounting for almost a third (156 $Å^2$) of the total buried surface area. Together with Ala12, Leu16, and Tyr17, it is accounting for over 60% (321 $Å^2$) of the interface. On $CheA_3P1$, the residues involved in the interaction with $CheY_6$ are slightly less clustered and spatially farther apart. Yet the three residues with the biggest contribution towards the total buried surface area, Val59 (103 $Å^2$, 20% of total buried surface area), Leu14 (64 $Å^2$, 12%), and Ile11 (48 $Å^2$, 9%), together account for almost half of the overall binding surface.

This analysis shows that only a small number of residues are necessary to form the majority of interactions within the complex. On $CheY_6$, these are all located on α1. Within this helix, Met13 has the most crucial role in the hydrophobic interaction. A sequence alignment of all identified RRs in *R. sphaeroides* shows that only $CheY_6$ and $CheB_2$ have a Met residue at position 13, whereas all others either have a Ser, Thr, or Ala at this position (Figure 4). As $CheA_3$-P serves as a phosphodonor for both $CheY_6$ and $CheB_2$ this suggests that Met13 has an important role in determining the specificity for binding to $CheA_3P1$.

## Substitution of M13 in $CheY_6$ Reduces Interaction and the Rate of Phosphotransfer from $CheA_3P1$-P

Residues 11–17 of $CheY_6$ collectively account for ~67% of the buried surface area of $CheY_6$ in the $CheA_3P1$-$CheY_6$ complex, with M13, L16, and Y17 each contributing ~30%, ~16%, and ~8%, respectively. To confirm that this surface of $CheY_6$ is involved in the interactions with $CheA_3P1$-P that lead to phosphotransfer in solution, we substituted residues at this surface to mimic those found in the noncognate RRs, $CheY_3$ and $CheY_4$. M13 was changed to S, and Y17 was changed to M as found in both $CheY_3$ and $CheY_4$. $CheY_3$ and $CheY_4$ both have C at position 16; however, it has previously been shown that $CheY_3$(C16S) and $CheY_4$(C16S) behave indistinguishably from $CheY_3$ and $CheY_4$ in phosphotransfer assays (S. L. Porter, unpublished data), and therefore, to avoid any potential problems from disulphide bond formation during the purification, we

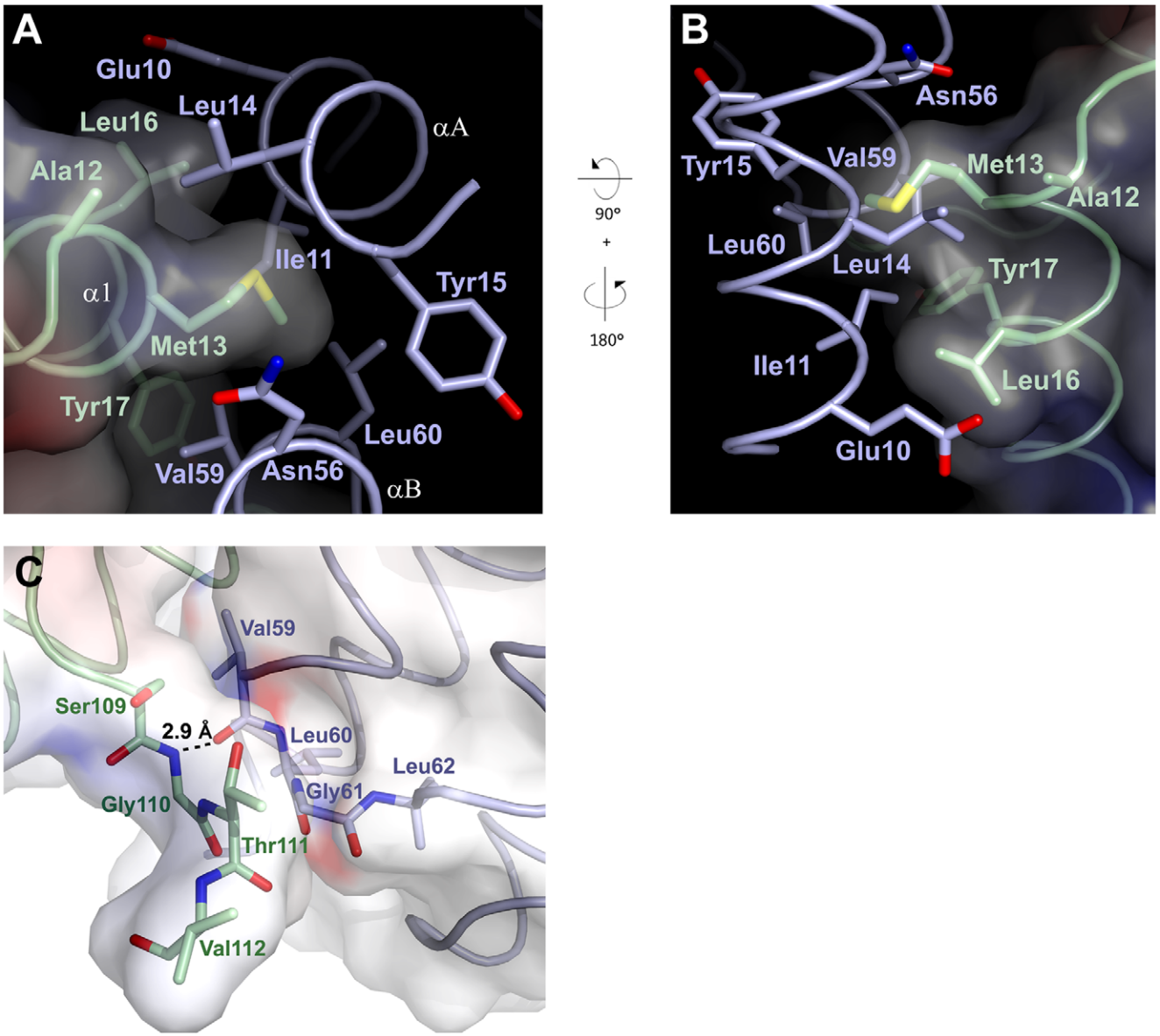


**Figure 3. Close-up view of the two binding sites between $CheA_3P1$ and $CheY_6$.** Colour coding as in Figure 1. Residues that are involved in the interaction are shown in stick representation. (A) Detailed view onto the major binding site between $CheY_6$ and $CheA_3P1$. Orientation as in Figure 1B, residues 19–53 of $CheA_3$ P1 are omitted for clarity. (B) Solvent accessible surface of $CheY_6$ coloured by electrostatic potential contoured at ±10 kT. Met13 fits snugly into the hydrophobic pocket on $CheA_3P1$. (C) Close-up view onto the second binding site. Orientation as in Figure 1A. The solvent-accessible surface area is coloured by electrostatic potential contoured at ±10 kT. The hydrogen bond between Gly110 of $CheY_6$ and Val59 of $CheA_3P1$ is marked with a dotted line.
doi:10.1371/journal.pbio.1000306.g003

changed L16 to S rather than C. Two mutant proteins were produced, $CheY_6$(M13S) and $CheY_6$(M13S,L16S,Y17M).

Surface plasmon resonance (SPR) assays showed that wild-type $CheY_6$ binds to $CheA_3P1$ with an affinity of 218 μM (Figure 5). This weak interaction is in agreement with the transient nature of the complex and the small buried surface area between the two proteins as observed in the crystal structure. Both the single-mutant protein, $CheY_6$(M13S), and the triple-mutant protein $CheY_6$(M13S,L16S,Y17M) showed a remarkable decrease in affinity, with a $K_d$ of more than 1 mM (Figure 5 and Figure S3).

Consistent with the SPR binding assays, the rate of phosphotransfer from $CheA_3P1$-P to each of the two mutant $CheY_6$ proteins was much slower than to wild-type $CheY_6$ (Figure 6A–6C), with phosphotransfer to the triple-mutant protein $CheY_6$(M13S,L16S,Y17M) being slowest. These results underline the conclusions drawn from the structural characterization of the complex and stress the importance of the Met finger at position 13 for binding of $CheY_6$ to $CheA_3P1$. In addition, the hydrophobic interaction mediated by Leu16 and Tyr17 also adds significantly to recognition of $CheY_6$ by $CheA_3P1$.

## Reengineering $CheY_4$ into a Cognate RR of $CheA_3P1$-P

The sequence of $CheY_4$ is 36% identical to $CheY_6$; however, unlike $CheY_6$, $CheY_4$ is not a cognate RR of $CheA_3P1$-P (Figure 6D). Consistent with this, SPR assays failed to detect a significant interaction between $CheA_3P1$ and $CheY_4$ (Figure 5).

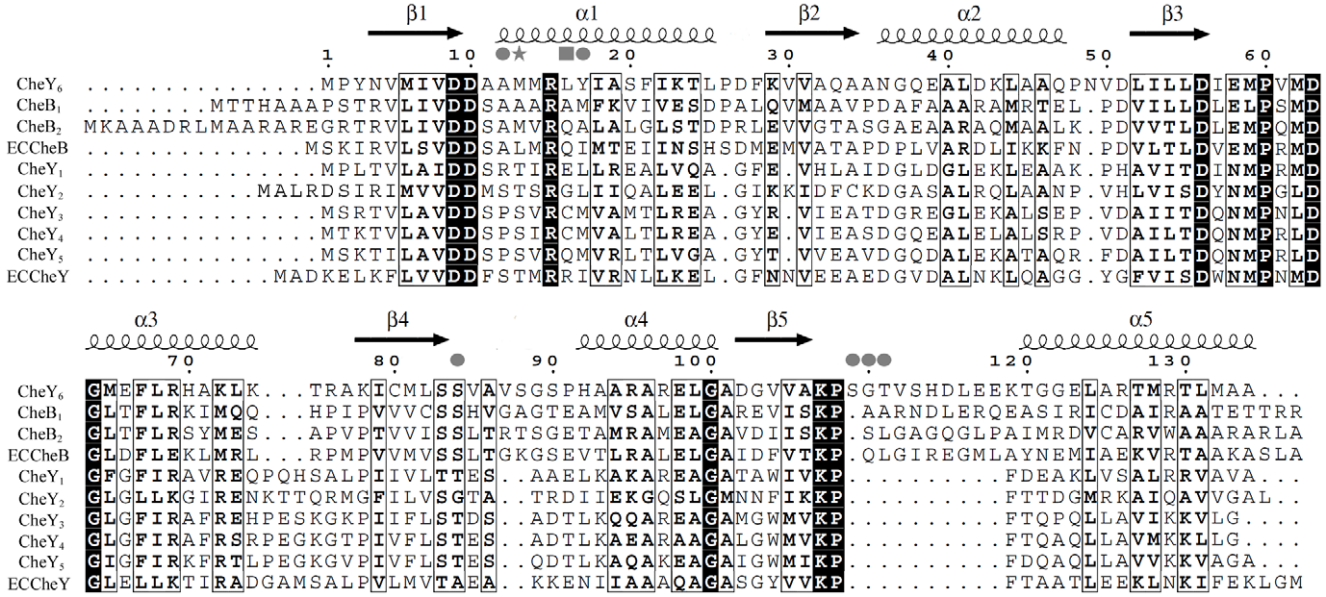


**Figure 4. Structure-guided sequence alignment of the chemotaxis RRs from *E. coli* and *R. sphaeroides*.** Alignment is based on the structures of *E. coli* CheY (PDB code: 3CHY), *E. coli* CheB (1A2O), *R. sphaeroides* $CheY_3$ (C. H. Bell, unpublished data), and *R. sphaeroides* $CheY_6$. Secondary structure is shown for $CheY_6$. Residues involved in binding of $CheY_6$ to $CheA_3P1$ are marked with a star (contributes >30% to total buried surface area), square (>15%), or circle (>5%).
doi:10.1371/journal.pbio.1000306.g004

**A**

| Interaction | $K_d$ [μM] |
|---|---|
| $CheA_3$ P1 - $CheY_6$ wt | 218 ± 8 |
| $CheA_3$ P1 - $CheY_6$(M13S) | > 1000 |
| $CheA_3$ P1 - $CheY_6$(M13S,L16S,Y17M) | > 1000 |
| $CheA_3$ P1 - $CheY_4$ wt | ND |
| $CheA_3$ P1 - $CheY_4$(P12A,S13M) | 678 ± 34 |
| $CheA_3$ P1 - $CheY_4$(P12A,S13M,C16L,M17Y) | 365 ± 35 |

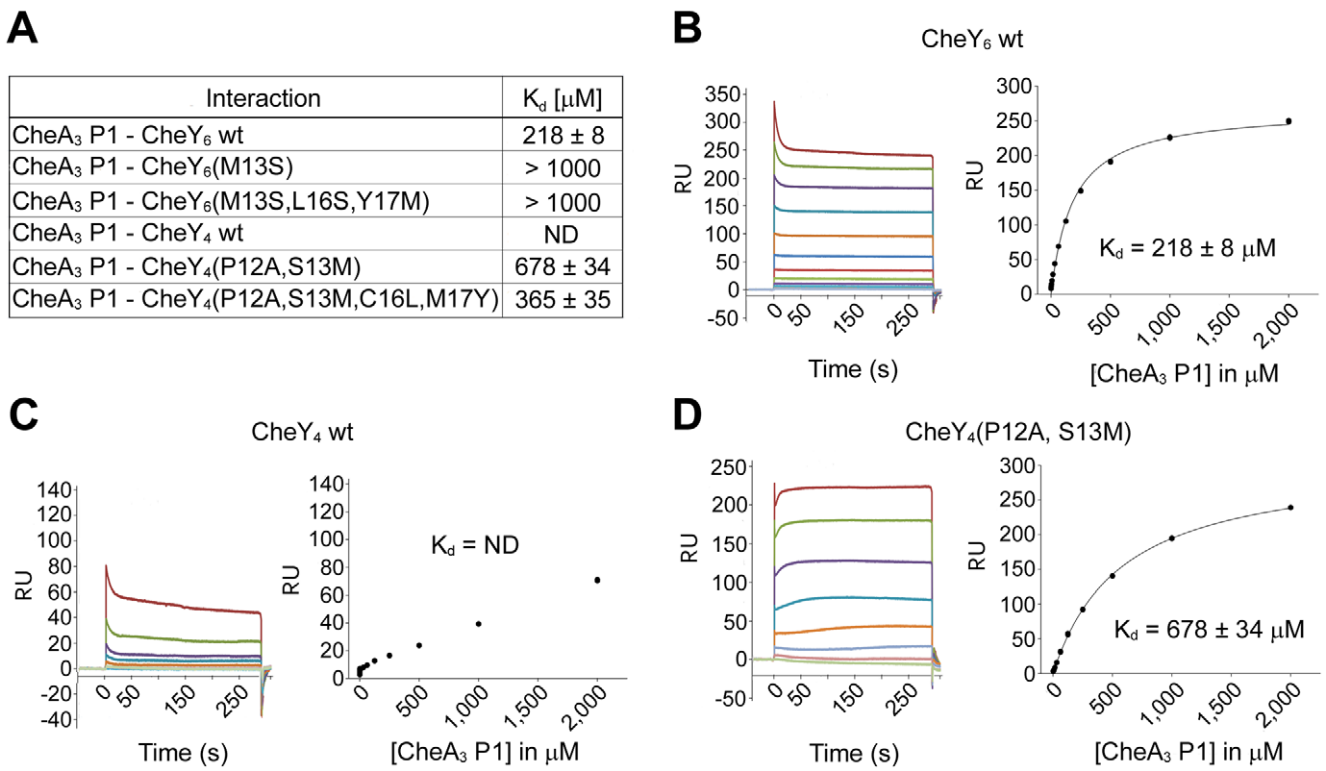


**Figure 5. Binding of $CheA_3P1$ to the response regulators.** (A) Table of binding constants ($K_d$) measured by SPR between $CheA_3P1$ and $CheY_4$, $CheY_6$ and their mutant versions. Data are expressed as mean ± standard error of the mean (s.e.m.). ND, not determinable. (B–D) Binding of $CheA_3P1$ to $CheY_6$ wild type (wt), $CheY_4$ wt, and $CheY_4$(P12A,S13M). Left, representative sets of experimental sensorgrams from typical equilibrium-based binding experiments, with reference subtraction. Different concentrations of $CheA_3P1$ were injected over surfaces coupled with the respective RR. For all injections, the experimental traces reached equilibrium and returned to baseline after the injection. Right, plot of the equilibrium binding response (response units [RU]) against $CheA_3P1$ concentration ranging from 120 nM to 2 mM. Within one experiment, each concentration was measured twice. All experiments were performed in duplicate. Best-fit binding curves corresponding with a 1:1 binding model are shown as lines.
doi:10.1371/journal.pbio.1000306.g005

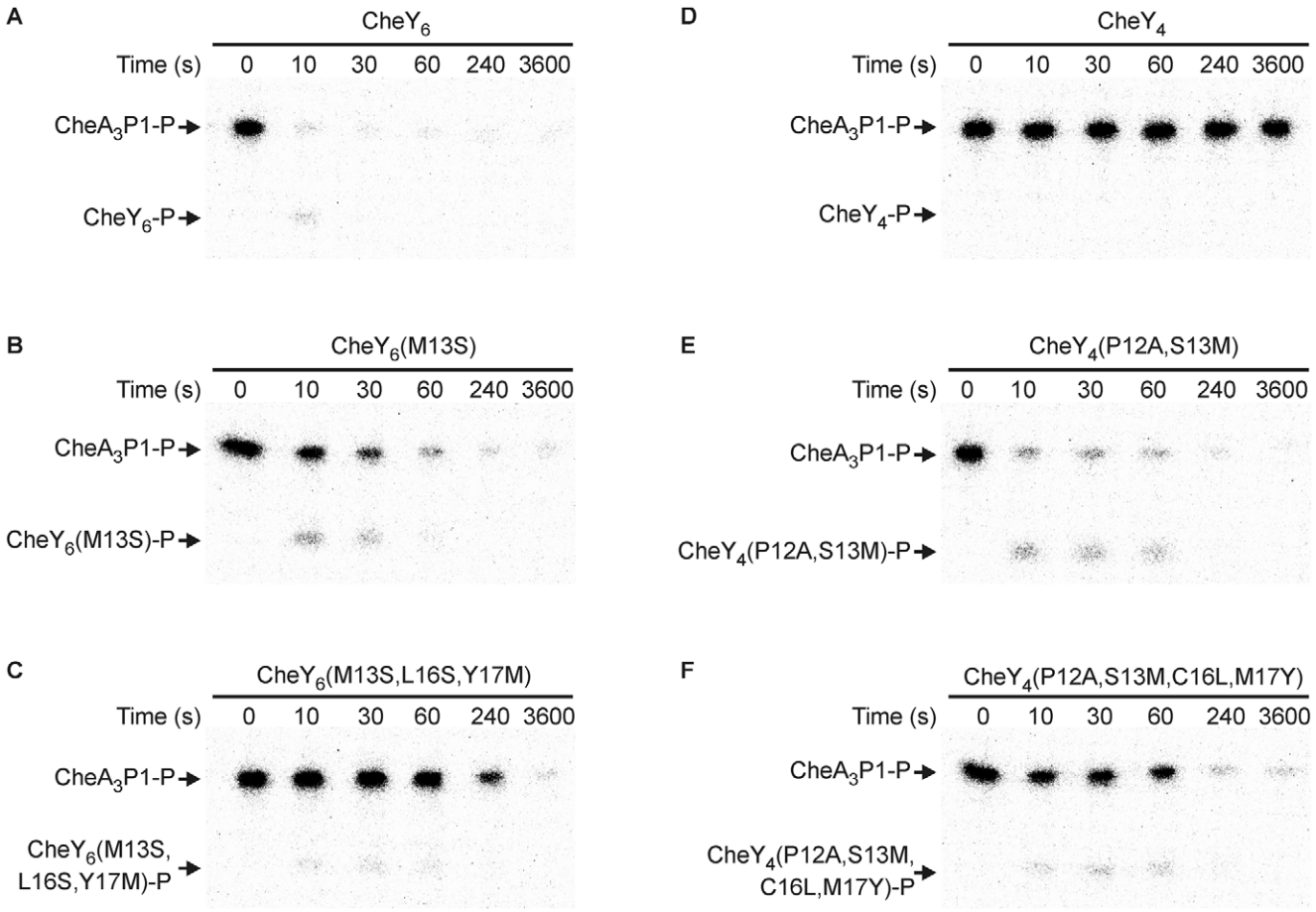


**Figure 6. Changing the phosphotransfer specificity of $CheY_6$ and $CheY_4$.** Phosphorimages of SDS-PAGE gels measuring phosphotransfer from $CheA_3P1$-P to (A) $CheY_6$, (B) $CheY_6$(M13S), (C) $CheY_6$(M13S,L16S,Y17M), (D) $CheY_4$, (E) $CheY_4$(P12A,S13M), and (F) $CheY_4$(P12A,S13M,C16L,M17Y). CheY (5 μM) was added to 1 μM $CheA_3P1$-$^{32}P$. Ten-microlitre reaction samples were taken at the time points indicated and quenched in 20 μl of 1.5× SDS/EDTA loading dye. The quenched samples were analyzed by SDS-PAGE and detected by phosphorimaging.
doi:10.1371/journal.pbio.1000306.g006

In an attempt to alter the phosphotransfer specificity of $CheY_4$ to allow phosphotransfer from $CheA_3P1$-P, we substituted the $CheY_4$ residues corresponding to the positions shown to interact in the $CheA_3P1$-$CheY_6$ structure, so that they matched $CheY_6$. Two mutant proteins were produced: $CheY_4$(P12A,S13M) and $CheY_4$(P12A,S13M,C16L,M17Y). Ala12 was included in both mutant proteins since $CheY_4$ has a Pro at position 12 that might influence the orientation of α1 and thus interfere with the proper positioning of Met13 for interaction with the hydrophobic pocket. SPR assays showed that both mutant proteins bind $CheA_3P1$ (Figure 5 and Figure S3), and in phosphotransfer assays, both mutant proteins were phosphorylated by $CheA_3P1$-P (Figure 6E and 6F). Phosphotransfer was fastest from $CheA_3P1$-P to $CheY_4$(P12A,S13M), with most of the initial $CheA_3P1$-P dephosphorylated within 10 s (Figure 6E).

Interestingly, although the rate of phosphotransfer from $CheA_3P1$-P to $CheY_4$(P12A,S13M) was faster than to $CheY_4$(-P12A,S13M,C16L,M17Y), the SPR results show that $CheA_3P1$ interacts slightly more strongly with $CheY_4$(P12A,S13M, C16L,M17Y) than with $CheY_4$(P12A,S13M) (Figure 5 and Figure S3). This apparent discrepancy could be explained by the alignment of the phosphorylated histidine and the phosphorylatable aspartate in the $CheY_4$(P12A,S13M,C16L,M17Y).$CheA_3P1$-P complex, which might be slightly less optimal for catalysis than in the $CheY_4$(P12A,S13M).$CheA_3P1$-P complex. Nevertheless, both methods show that mutating $CheY_4$ so that it resembles $CheY_6$ at the contact sites with $CheA_3P1$ enhances both binding affinity and phosphotransfer rate. These results demonstrate that substitution of just two residues is sufficient to change the phosphotransfer specificity of $CheY_4$.

## Reengineering Other CheYs

Having successfully reengineered the phosphotransfer specificity of $CheY_4$ by introducing A12 and M13, we used the same approach to change the specificity of $CheY_1$, $CheY_3$, $CheY_5$, and *E. coli* CheY (Figure 7). These proteins share between 30% and 33% sequence identity with $CheY_6$. In all cases, the mutant proteins containing the alanine and methionine substitutions were phosphorylated more rapidly by $CheA_3P1$-P than were their wild-type counterparts. Although $CheY_1$ and *E. coli* CheY both lack a methionine residue at the position corresponding to M13 of $CheY_6$, they are both phosphorylated by $CheA_3P1$-P (Figure 7A and 7C); however, phosphotransfer to their corresponding alanine and methionine substitution mutant proteins proceeded even faster, with almost complete dephosphorylation of $CheA_3P1$-P within 10 s (Figure 7B and 7D). Similar to $CheY_4$, wild-type $CheY_3$ and $CheY_5$ were not phosphorylated by $CheA_3P1$-P

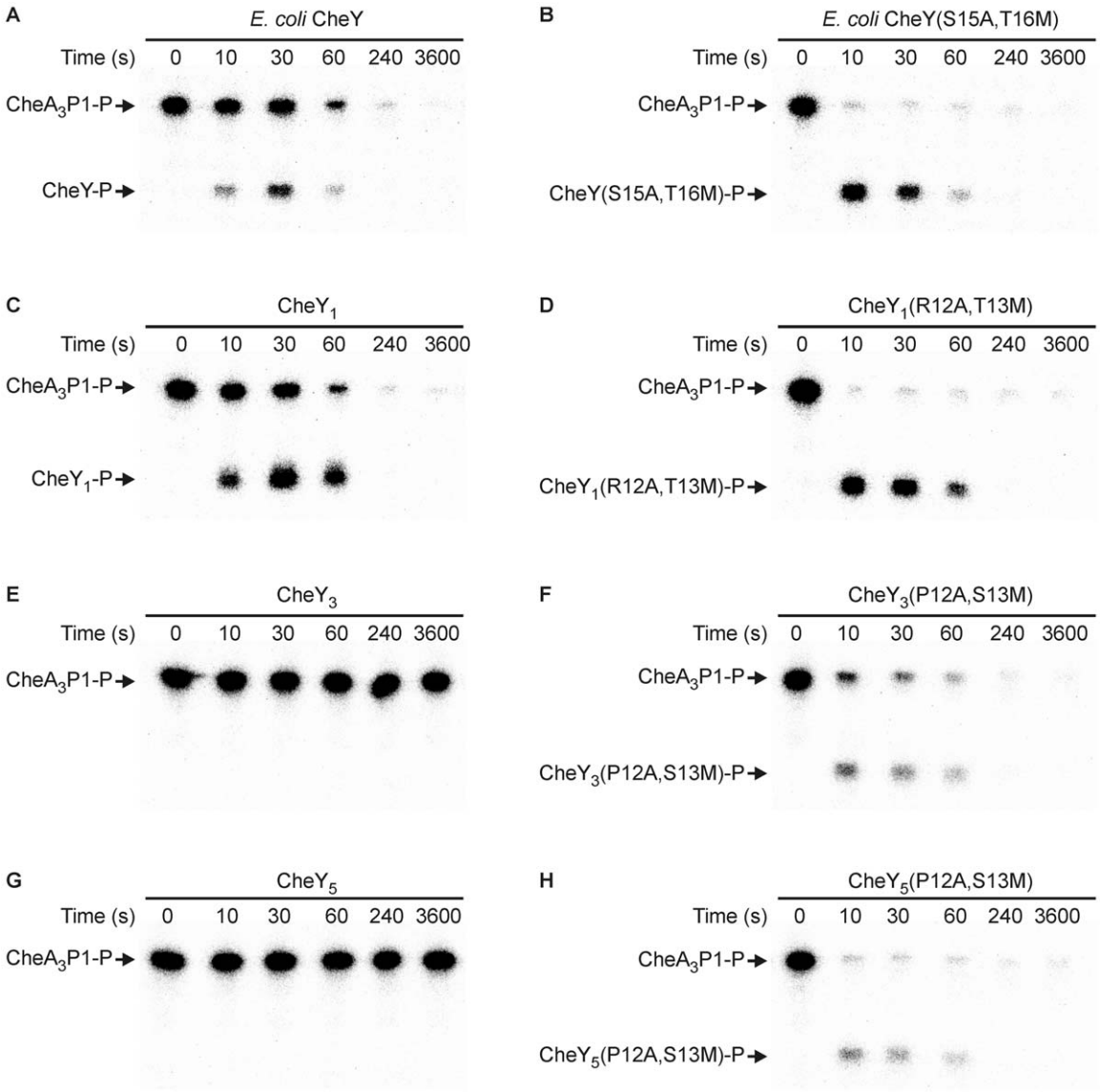


**Figure 7. Changing the phosphotransfer specificity of other CheYs by introduction of A12 and M13.** Phosphorimages of SDS-PAGE gels measuring phosphotransfer from $CheA_3P1$-P to (A) *E. coli* CheY, (B) *E. coli* CheY(S15A,T16M), (C) $CheY_1$, (D) $CheY_1$(R12A,T13M), (E) $CheY_3$, (F) $CheY_3$(P12A,S13M), (G) $CheY_5$, and (H) $CheY_5$(P12A,S13M). CheY (5 μM) was added to 1 μM $CheA_3P1$-$^{32}P$. Ten-microlitre reaction samples were taken at the time points indicated and quenched in 20 μl of 1.5× SDS/EDTA loading dye. The quenched samples were analyzed by SDS-PAGE and detected by phosphorimaging.
doi:10.1371/journal.pbio.1000306.g007

(Figure 7E and 7G), and the effect of the alanine and methionine substitutions was to allow rapid phosphotransfer from $CheA_3P1$-P (Figure 7F and 7H). These results demonstrate that the RR residues at the positions equivalent to A12 and M13 of $CheY_6$ play a major role in determining phosphotransfer specificity.

## Discussion

Two-component signalling systems depend on a high level of selectivity between histidine kinases and their cognate RRs to prevent cross-talk between different pathways. Here, we present structural and functional data that elucidate how this specificity is mediated on a molecular level. We identified the key residues for molecular recognition and thereby were able to reengineer phosphotransfer specificity. Considering the high level of structural homology within the receiver and Hpt domain families, the presented structure together with complementary information, e.g., analysis of amino acid covariation [28,36,37], is likely to facilitate the rational reengineering of CheA-like histidine kinase–RR pairs for use, for example, in synthetic signalling circuits.

### Conserved Features of the $CheA_3P1.CheY_6$ Complex

The structure of $CheA_3P1$ in complex with $CheY_6$ is, to our knowledge, the first structure of a Hpt domain of a CheA protein in complex with a RR. To date, there are only two other structures of a Hpt domain in complex with a RR, namely Spo0B/Spo0F [38,39] from *Bacillus subtilis* and YPD1/SLN1 [40,41] from *Saccharomyces cerevisiae*. Although the overall structure of the RR is well conserved in all three complexes, there are remarkable differences in the Hpt domains. Spo0B exists as a dimer in which the two α-helices of the helical hairpin domain of each protomer

associate to form a four-helix bundle. In addition, Spo0B has a C-terminal domain with an $\alpha/\beta$ fold, which is involved in binding of the RR. YPD1 is a monomeric Hpt protein consisting of a four-helix bundle with an additional short helix at the N-terminus. This N-terminal helix is involved in RR binding and complements the interface formed by helices αB and αC. When the three complexes were superimposed with respect to the receiver domains, $CheA_3P1$ aligned well with YPD1 but only poorly with Spo0B (Figure S4).

### Phosphotransfer Specificity Determinants

$CheA_3P1.CheY_6$ shows the smallest binding interface amongst the three complexes solved so far, with 530 $Å^2$ compared to 953 $Å^2$ in YPD1/SLN1 and 1,200 $Å^2$ in Spo0F/Spo0B. The interface is smaller since $CheA_3P1$ has neither the C-terminal $\alpha/\beta$ fold domain seen in Spo0B nor the additional N-terminal helix seen in YPD1. Despite this small interface, $CheA_3P1$ shows binding and efficient phosphotransfer to $CheY_6$. It was previously proposed that the P2 domain of CheA-like proteins might be necessary for binding of the RR to CheA by increasing the binding interface [40]. However, $CheA_3$ does not have a P2 domain, and the experimental data presented here and elsewhere [26] show that the P1 domain alone is sufficient for binding of and specific phosphotransfer to the cognate RR. Moreover, the structural and mutational analysis suggests that their interaction is mediated by very distinct residue clusters on the RR and the Hpt domain, the former being located on the N-terminal region of α1 and the loop region between β5 and α5, and the latter being located on the N- and C-terminal region of αA and αB, respectively, and the loop region connecting αB and αC. This is in good agreement with a recently published computational analysis of amino acid coevolution of cognate histidine kinase–RR pairs [28] and the binding site found in the YPD1/SLN1 [40,41] or Spo0B/Spo0F [38,39] complex.

### Reengineering Phosphotransfer Specificity

The specificity of protein–protein interactions is essential for most cellular processes. Despite the vast number of these interactions, our understanding of the molecular basis of their specificity is limited. The structure presented here has allowed us to identify specificity determinants for the CheA–CheY interaction. We successfully used this information to redesign noncognate RRs to allow them to be rapidly phosphorylated by $CheA_3P1$-P (Figures 6 and 7). Whereas the Laub group have reengineered a HPK to specifically phosphorylate non-cognate RR substrates [28], we have now shown that it is possible to rationally reengineer a RR so that it can be phosphorylated by a noncognate HPK. The changing of phosphotransfer specificity described here represents, to our knowledge, the first example of the redesign of the intracellular part of the chemotaxis pathway and provides valuable insight into how cells mediate specificity in one of the most abundant signal transduction pathways, two-component signalling. The ability to reengineer phosphotransfer specificity coupled with recent work from the Bourret group [42], which has shown that RR autodephosphorylation rate can be manipulated, provide a platform for the future design of synthetic two-component circuits with customizable kinetics.

## Materials and Methods

### Protein Overexpression and Purification

$CheA_3P1$ (residues 1–135 of $CheA_3$, GenBank ID 3720125), $CheY_6$ (GenBank ID 3720126), and $CheY_4$ (GenBank ID 3722004) were cloned into the bacterial expression vector pQE80 (Qiagen), which includes an N-terminal $His_6$-tag. Sequence verified plasmids were transformed into M15pREP4 cells (Qiagen) and cultivated in Terrific Broth to an absorbance at 600 nm ($A_{600}$) of 0.8. Cultures were cooled to 20°C, induced with 0.25 mM IPTG, and then grown for ~15 h before harvesting. The bacterial pellets were resuspended in 25 mM sodium phosphate (pH 8.0), 500 mM NaCl, 0.5 mM β-mercaptoethanol, and EDTA-free protease inhibitor cocktail (Roche). Cells were lysed using a Basic Z model cell disruptor (Constant Systems) and fractionated by centrifugation (45,000*g*, 4°C, 60 min). $CheA_3P1$, $CheY_6$, and $CheY_4$ were purified from the supernatant by immobilized metal-affinity chromatography [19–21]. The samples were dialysed against standard buffer (30 mM Hepes [pH 7.5], 150 mM NaCl, 5 mM sodium acetate, 2 mM manganese chloride, 2 mM Tris(2-carboxyethyl)phosphine [TCEP]) and further purified by size-exclusion chromatography. Protein purity and concentration was measured as described [43]. Purified proteins were stored at −80°C. Seleno-methionine (SeMet)-labelled $CheY_6$ was produced essentially as described [44]. The complex between $CheY_6$ and $CheA_3P1$ was formed by mixing equimolar amounts of both proteins. The sample was incubated for 30 min at room temperature (20°C), and the complex was purified by size-exclusion chromatography. $CheA_3P1$ was phosphorylated using ATP and $CheA_4$, and purified as described previously [26]. The final preparation of $CheA_3P1$-P was free of ATP and $CheA_4$. Phosphorylation was verified by mass spectrometry. Equimolar amounts of phosphorylated $CheA_3P1$ and $CheY_6$(D56N,S83A) were mixed and set up for crystallization.

### Site-Directed Mutagenesis

Mutations were introduced using the Quikchange Site-Directed Mutagenesis Kit (Stratagene).

### Crystallization and Data Collection

Crystal trials were set up with the purified $CheA_3P1.CheY_6$ complex at a concentration of 20 mg/ml. We set up nanoliter crystallization trials using a Cartesian Technologies robot (100 nl of protein solution plus 100 nl of reservoir solution) in 96-well Greiner plates [45], placed them in a TAP (The Automation Partnership) Homebase storage vault maintained at 295 K, and imaged them via a Veeco visualization system. Crystals of the phosphorylated, unphosphorylated and SeMet-labelled complex between $CheY_6$ and $CheA_3P1$ could be obtained in 100 mM Bicine (pH 9), 1 M LiCl, 20% (w/v) PEG6000. Crystals were optimized using a dilution series of the initial condition. Crystals reached their final size of $400\times100\times100$ $\mu m^3$ after 12 h.

Diffraction data were collected at 100 K, crystals being flash-cooled in a cryo $N_2$ gas stream. Before flash-freezing, crystals were cryo-protected with perfluoropolyether oil PFO-X125/03 (Lancaster Synthesis). The native dataset was collected at beamline I03 ($\lambda = 0.9757$ Å) and the SeMet dataset at beamline I04 ($\lambda = 0.979$ Å) at the Diamond Light Source. Data for the phosphorylated complex were collected on a MAR345 detector (Marresearch) mounted on a Miromax007 generator (Rigaku), equipped with Varimax HR Osmic mirrors (Rigaku). X-ray data were processed and scaled with the HKL suite [46]. Data collection statistics are shown in Table 1.

### Structure Determination and Refinement

The $CheA_3P1$-$CheY_6$ complex structure was determined by SAD analysis. The positions of 12 selenium atoms were determined by using SHELXD [47]. This solution was put into AUTOSHARP [48] for phase calculation, improvement, and phase extension using the high-resolution native data to 1.4 Å resolution. The resulting map was of high quality and allowed

tracing of the whole polypeptide chain. An initial model was built automatically using Arp/wARP [49] and manually adjusted using COOT [50]. The structure was refined using autoBUSTER [51], REFMAC [52], and Phenix [53]. The phosphorylated complex was solved by molecular replacement using Phaser [54] with the unphosphorylated complex as model.

Refinement statistics are given in Table 1; all data within the indicated resolution range were included. Stereochemical properties were assessed by MOLPROBITY [55] and PROCHECK [56]. Ramachandran statistics are as follows (favored/disallowed, %): $CheA_3P1$-$CheY_6$ unphosphorylated 98.8/0, $CheA_3P1$-$CheY_6$ phosphorylated 99.1/0. Superpositions were calculated using lsqkab [57] implemented in the CCP4 suite and electrostatic potentials were generated using APBS [58]. Buried surface areas of protein–protein interactions were calculated using the PISA Webserver (http://www.ebi.ac.uk/msd-srv/prot_int/pistart.html). Coordinates are deposited in RSCB Data Bank under 3KYI and 3KYJ.

### Surface Plasmon Resonance Binding Studies

SPR experiments were performed using a Biacore T100 machine (GE Healthcare) at 25°C in standard buffer supplemented with 0.05% (v/v) Tween 20. Protein concentrations were determined from the absorbance at 280 nm using calculated molar extinction coefficients. Proteins for surface attachment were enzymatically biotinylated within an engineered C-terminal tag. These proteins were then attached to surfaces on which 3,000 response units (RU) of streptavidin were coupled via primary amines [59] yielding a density of 200–1,500 RU of biotinylated protein. All experiments were done in duplicates with independently purified proteins. The signal from experimental flow cells was corrected by subtraction of a blank and reference signal from a mock or irrelevant protein-coupled flow cell. In all experiments analyzed, the experimental trace returned to baseline after each injection and the data fitted to a simple 1:1 Langmuir model of binding. $K_d$ values were obtained by nonlinear curve fitting of the Langmuir binding isotherm (bound = Cmax/($K_d$ + C), where C is analyte concentration and max is the maximum analyte binding) evaluated using the Biacore Evaluation software (GE Healthcare).

### Detection of Phosphotransfer from $CheA_3P1$-P to the RRs

Assays were performed at 20°C in TGMNKD buffer (50 mM Tris HCl, 10% [v/v] glycerol, 5 mM $MgCl_2$, 150 mM NaCl, 50 mM KCl, 1 mM DTT [pH 8.0]). $CheA_3P1$ was phosphorylated using [$\gamma$-$^{32}$P] ATP and $CheA_4$, and purified as described previously [26]. The final preparation of $CheA_3P1$-$^{32}$P was free of ATP and $CheA_4$. $CheA_3P1$-$^{32}$P (1 μM) was mixed with 5 μM RR in a final reaction volume of 100 μl. Following the addition of RR, reaction aliquots of 10 μl were taken at the indicated time points and quenched immediately in 20 μl of 1.5× SDS-PAGE loading dye (3.75% [w/v] SDS, 45 mM EDTA, 18.75 mM Tris HCl, 18.75% [v/v] glycerol, 1.5% [v/v] β-mercaptoethanol [pH 6.8]). Quenched samples were analyzed using SDS-PAGE and phosphorimaging as described previously [21].

## Supporting Information

**Figure S1 Stereoview of a superposition of the metal binding site of $CheY_6$ and *E. coli* CheY.** $CheY_6$ is shown in pale green, *E. coli* CheY with $Mg^{2+}$ bound (PDB-code: 1CHN) in yellow, and *E.coli* CheY without $Mg^{2+}$ (3CHY) in teal. Structures were aligned on their secondary structure elements using secondary structure matching (SSM) implemented in COOT [50]. Residues involved in the coordination of $Mg^{2+}$ in *E. coli* CheY are shown in stick representation for all three structures. Residues in *E. coli* structures are only labelled for the $Mg^{2+}$ bound form. $Mg^{2+}$ from the *E. coli* structure is shown as a grey sphere. $CheY_6$ resembles the $Mg^{2+}$ bound form of *E. coli* CheY despite not having a divalent cation bound to its metal binding site.
Found at: doi:10.1371/journal.pbio.1000306.s001 (6.24 MB TIF)

**Figure S2 Electron density of phosphorylated His51 in $CheA_3P1$ in the active complex structure.** The orientation is similar to Figure 2B. The density represents a 2*Fobs-Fcalc* map contoured at 1.5 σ and calculated after initial rigid body refinement in Phaser [54] and one round of positional refinement in autoBUSTER [51], both omitting the phosphate group from the model.
Found at: doi:10.1371/journal.pbio.1000306.s002 (0.64 MB TIF)

**Figure S3 Binding of $CheA_3P1$ to substitution mutants of $CheY_4$ and $CheY_6$.** (A–C) Binding of $CheA_3P1$ to $CheY_4$(P12A,S13M,C16L,M17Y), $CheY_6$(M13S), and $CheY_6$(M13S,L16S,Y17M). Left, representative sets of experimental sensorgrams from typical equilibrium-based binding experiments, with reference subtraction. Different concentrations of $CheA_3P1$ were injected over surfaces coupled with the respective RR. For all injections, the experimental traces reached equilibrium and returned to baseline after the injection. Right, plot of the equilibrium binding response (response units [RU]) against $CheA_3P1$ concentration ranging from 120 nM to 2 mM. Within one experiment, each concentration was measured twice. All experiments were performed in duplicate. Best-fit binding curves corresponding with a 1:1 binding model are shown as lines. Experiments with $CheY_6$(M13S) and $CheY_6$(M13S,L16S,Y17M) did not reach saturation due to very low affinity, thus the $K_d$ value is estimated.
Found at: doi:10.1371/journal.pbio.1000306.s003 (0.52 MB TIF)

**Figure S4 Superposition of the $CheA_3P1$-$CheY_6$ complex structure with the Spo0B-Spo0F complex and YPD1-SLN1 complex.** (A) Superposition of $CheA_3P1$-$CheY_6$ with Spo0B-Spo0F (PDB-code: 1F51). (B) Superposition of $CheA_3P1$-$CheY_6$ with YPD1-SLN1 (1OXB). All structures were superimposed on the RRs using SSM as implemented in COOT [50]. $CheY_6$ is shown in pale green, CheA3P1 in light blue, Spo0F in orange, Spo0B in teal, SLN1 in purple, and YPD1 in aquamarine. Only the four-helix bundle of the Spo0B dimer is shown; the C-terminal domain is omitted for clarity. The orientation is similar to Figure 1. $CheA_3P1$ is structurally more similar to the monomeric YPD1 than to Spo0B.
Found at: doi:10.1371/journal.pbio.1000306.s004 (2.64 MB TIF)

## Acknowledgments

We thank the staff of Diamond beamlines I03 and I04 for assistance with data collection, T. Walter for help with crystallization, and K. Harlos for help with data collection. We acknowledge the use of the crystallization facilities provided by the Medical Research Council (MRC)–funded Oxford Protein Production Facility (OPPF).

## Author Contributions

The author(s) have made the following declarations about their contributions: Conceived and designed the experiments: SLP JPA. Analyzed the data: CHB SLP DIS. Wrote the paper: CHB SLP DIS JPA. Produced the constructs; crystallized the protein complexes and solved the structures; designed the CheY6 and CheY4 mutant proteins; carried out the SPR experiments: CHB. Designed the CheY6 and CheY4 mutant proteins; performed the phosphotransfer assays: SLP. Produced the constructs: AS.

## References


1. West AH, Stock AM (2001) Histidine kinases and response regulator proteins in two- component signaling systems. Trends Biochem Sci 26: 369–376.
2. Stock AM, Robinson VL, Goudreau PN (2000) Two-component signal transduction. Annu Rev Biochem 69: 183–215.
3. Laub MT, Goulian M (2007) Specificity in two-component signal transduction pathways. Ann Rev Genet 41: 121.
4. Siryaporn A, Goulian M (2008) Cross-talk suppression between the CpxA-CpxR and EnvZ-OmpR two-component systems in *E. coli*. Mol Microbiol 70: 494–506.
5. Skerker JM, Prasol MS, Perchuk BS, Biondi EG, Laub MT (2005) Two-component signal transduction pathways regulating growth and cell cycle progression in a bacterium: a system-level analysis. PLoS Biology 3: e334. doi:10.1371/journal.pbio.0030334.
6. Casino P, Rubio V, Marina A (2009) Structural insight into partner specificity and phosphoryl transfer in two-component signal transduction. Cell 139: 325–336.
7. Hess JF, Bourret RB, Simon MI (1988) Histidine phosphorylation and phosphoryl group transfer in bacterial chemotaxis. Nature 336: 139–143.
8. Bourret RB, Hess JF, Simon MI (1990) Conserved aspartate residues and phosphorylation in signal transduction by the chemotaxis protein CheY. Proc Natl Acad Sci U S A 87: 41–45.
9. Tindall MJ, Maini PK, Porter SL, Armitage JP (2008) Overview of mathematical approaches used to model bacterial chemotaxis II: bacterial populations. Bull Math Biol 70: 1570–1607.
10. Tindall MJ, Porter SL, Maini PK, Gaglia G, Armitage JP (2008) Overview of mathematical approaches used to model bacterial chemotaxis I: the single cell. Bull Math Biol 70: 1525–1569.
11. Hazelbauer GL, Falke JJ, Parkinson JS (2008) Bacterial chemoreceptors: high-performance signaling in networked arrays. Trends Biochem Sci 33: 9–19.
12. Baker MD, Wolanin PM, Stock JB (2006) Signal transduction in bacterial chemotaxis. Bioessays 28: 9–22.
13. Porter SL, Wadhams GH, Armitage JP (2008) *Rhodobacter sphaeroides*: complexity in chemotactic signalling. Trends Microbiol 16: 251–260.
14. Wadhams GH, Armitage JP (2004) Making sense of it all: bacterial chemotaxis. Nat Rev Mol Cell Bio 5: 1024–1037.
15. Hamer R, Chen P-Y, Armitage JP, Reinert G, Deane CM (2010) Deciphering chemotaxis pathways using cross species comparisons. BMC Syst Biol 4: 3.
16. del Campo AM, Ballado T, de la Mora J, Poggio S, Camarena L, et al. (2007) Chemotactic control of the two flagellar systems of *Rhodobacter sphaeroides* is mediated by different sets of CheY and FliM proteins. J Bacteriol 189: 8397–8401.
17. Shah DS, Porter SL, Harris DC, Wadhams GH, Hamblin PA, et al. (2000) Identification of a fourth cheY gene in *Rhodobacter sphaeroides* and interspecies interaction within the bacterial chemotaxis signal transduction pathway. Mol Microbiol 35: 101–112.
18. Shah DSH, Porter SL, Martin AC, Hamblin PA, Armitage JP (2000) Fine tuning bacterial chemotaxis: analysis of *Rhodobacter sphaeroides* behaviour under aerobic and anaerobic conditions by mutation of the major chemotaxis operons and cheY genes. EMBO J 19: 4601–4613.
19. Porter SL, Wadhams GH, Martin AC, Byles ED, Lancaster DE, et al. (2006) The CheYs of *Rhodobacter sphaeroides*. J Biol Chem 281: 32694–32704.
20. Porter SL, Armitage JP (2004) Chemotaxis in *Rhodobacter sphaeroides* requires an atypical histidine protein kinase. J Biol Chem 279: 54573–54580.
21. Porter SL, Armitage JP (2002) Phosphotransfer in *Rhodobacter sphaeroides* chemotaxis. J Mol Biol 324: 35–45.
22. Martin AC, Wadhams GH, Shah DSH, Porter SL, Mantotta JC, et al. (2001) CheR- and CheB-dependent chemosensory adaptation system of *Rhodobacter sphaeroides*. J Bacteriol 183: 7135–7144.
23. Wadhams GH, Warren AV, Martin AC, Armitage JP (2003) Targeting of two signal transduction pathways to different regions of the bacterial cell. Mol Microbiol 50: 763–770.
24. Wadhams GH, Martin AC, Porter SL, Maddock JR, Mantotta JC, et al. (2002) TlpC, a novel chemotaxis protein in *Rhodobacter sphaeroides*, localizes to a discrete region in the cytoplasm. Mol Microbiol 46: 1211–1221.
25. Porter SL, Warren AV, Martin AC, Armitage JP (2002) The third chemotaxis locus of *Rhodobacter sphaeroides* is essential for chemotaxis. Mol Microbiol 46: 1081–1094.
26. Porter SL, Roberts MAJ, Manning CS, Armitage JP (2008) A bifunctional kinase-phosphatase in bacterial chemotaxis. Proc Natl Acad Sci U SA 105: 18531–18536.
27. Ind AC, Porter SL, Brown MT, Byles ED, de Beyer JA, et al. (2009) An inducible expression plasmid for *Rhodobacter sphaeroides* and *Paracoccus denitrificans*. Appl Environ Microbiol 75: 6613–6615.
28. Skerker JM, Perchuk BS, Siryaporn A, Lubin EA, Ashenberg O, et al. (2008) Rewiring the specificity of two-component signal transduction systems. Cell 133: 1043–1054.
29. Volz K, Matsumura P (1991) Crystal structure of *Escherichia coli* CheY refined at 1.7Å resolution. J Biol Chem 266: 15511.
30. Stock AM, Martinez-Hackert E, Rasmussen BF, West AH, Stock JB, et al. (1993) Structure of the $Mg^{2+}$-bound form of CheY and mechanism of phosphoryl transfer in bacterial chemotaxis. Biochemistry 32: 13375–13380.
31. Zhou H, Dahlquist FW (1997) Phosphotransfer site of the chemotaxis-specific protein kinase CheA as revealed by NMR. Biochemistry 36: 699–710.
32. Mourey L, Da Re S, Pedelacq JD, Tolstykh T, Faurie C, et al. (2001) Crystal structure of the CheA histidine phosphotransfer domain that mediates response regulator phosphorylation in bacterial chemotaxis. J Biol Chem 276: 31074–31082.
33. Quezada CM, Gradinaru C, Simon MI, Bilwes AM, Crane BR (2004) Helical shifts generate two distinct conformers in the atomic resolution structure of the CheA phosphotransferase domain from *Thermotoga maritima*. J Mol Biol 341: 1283–1294.
34. Stewart RC, Jahreis K, Parkinson JS (2000) Rapid phosphotransfer to CheY from a CheA protein lacking the CheY-binding domain. Biochemistry 39: 13157–13165.
35. Nooren IMA, Thornton JM (2003) Structural characterisation and functional significance of transient protein-protein interactions. J Mol Biol 325: 991–1018.
36. Weigt M, White RA, Szurmant H, Hoch JA, Hwa T (2009) Identification of direct residue contacts in protein–protein interaction by message passing. Proc Natl Acad Sci U S A 106: 67–72.
37. Szurmant H, Bobay BG, White RA, Sullivan DM, Thompson RJ, et al. (2008) Co-evolving motions at protein–protein interfaces of two-component signaling systems identified by covariance analysis. Biochemistry 47: 7782–7784.
38. Zapf J, Sen U, Madhusudan, Hoch JA, Varughese KI (2000) A transient interaction between two phosphorelay proteins trapped in a crystal lattice reveals the mechanism of molecular recognition and phosphotransfer in signal transduction. Structure 8: 851–862.
39. Varughese KI, Tsigelny I, Zhao H (2006) The crystal structure of Beryllofluoride Spo0F in complex with the phosphotransferase Spo0B represents a phospho-transfer pretransition state. J Bacteriol 188: 4970–4977.
40. Xu OP, Porter SW, West AH (2003) The yeast YPD1/SLN1 complex: insights into molecular recognition in two-component signaling systems. Structure 11: 1569–1581.
41. Zhao X, Copeland DM, Soares AS, West AH (2008) Crystal structure of a complex between the phosphorelay protein YPD1 and the response regulator domain of SLN1 bound to a phosphoryl analog. J Mol Biol 375: 1141–1151.
42. Thomas SA, Brewster JA, Bourret RB (2008) Two variable active site residues modulate response regulator phosphoryl group stability. Mol Microbiol 69: 453–465.
43. Porter SL, Wadhams GH, Armitage JP (2007) In vivo and in vitro analysis of the *Rhodobacter sphaeroides* chemotaxis signaling complexes. Method Enzymol 423: 392–413.
44. Hendrickson WA, Horton JR, Lemaster DM (1990) Selenomethionyl proteins produced for analysis by Multiwavelength Anomalous Diffraction (Mad): a vehicle for direct determination of 3-dimensional structure. EMBO J 9: 1665–1672.
45. Walter TS, Diprose JM, Mayo CJ, Siebold C, Pickford MG, et al. (2005) A procedure for setting up high-throughput nanolitre crystallization experiments. Crystallization workflow for initial screening, automated storage, imaging and optimization. Acta Crystallogr Sect D-Biol Crystallogr 61: 651–657.
46. Otwinowski Z, Minor W (1997) Processing of X-ray diffraction data collected in oscillation mode. Method Enzymol 276: 307–326.
47. Schneider TR, Sheldrick GM (2002) Substructure solution with SHELXD. Acta Crystallogr Sect D-Biol Crystallogr 58: 1772–1779.
48. Vonrhein C, Blanc E, Roversi P, Bricogne G (2007) Automated structure solution with autoSHARP. Methods Mol Biol 364: 215–230.
49. Langer G, Cohen SX, Lamzin VS, Perrakis A (2008) Automated macromolecular model building for X-ray crystallography using ARP/wARP version 7. Nat Protocols 3: 1171–1179.
50. Emsley P, Cowtan K (2004) Coot: model-building tools for molecular graphics. Acta Crystallogr Sect D-Biol Crystallogr 60: 2126–2132.
51. Blanc E, Roversi P, Vonrhein C, Flensburg C, Lea SM, et al. (2004) Refinement of severely incomplete structures with maximum likelihood in BUSTER-TNT. Acta Crystallogr Sect D-Biol Crystallogr 60: 2210–2221.
52. Murshudov GN, Vagin AA, Dodson EJ (1997) Refinement of macromolecular structures by the maximum-likelihood method. Acta Crystallogr Sect D-Biol Crystallogr 53: 240–255.
53. Adams PD, Grosse-Kunstleve RW, Hung LW, Ioerger TR, Mccoy AJ, et al. (2002) PHENIX: building new software for automated crystallographic structure determination. Acta Crystallogr Sect D-Biol Crystallogr 58: 1948–1954.
54. McCoy AJ, Grosse-Kunstleve RW, Storoni LC, Read RJ (2005) Likelihood-enhanced fast translation functions. Acta Crystallogr Sect D-Biol Crystallogr 61: 458–464.
55. Davis IW, Leaver-Fay A, Chen VB, Block JN, Kapral GJ, et al. (2007) MolProbity: all-atom contacts and structure validation for proteins and nucleic acids. Nucl Acids Res 35: W375–W383.
56. Laskowski RA, Macarthur MW, Moss DS, Thornton JM (1993) PROCHECK: a program to check the stereochemical quality of protein structures. J Appl Crystallogr 26: 283–291.
57. Kabsch W (1976) Solution for best rotation to relate 2 sets of vectors. Acta Crystallogr Sect A 32: 922–923.

58. Baker NA, Sept D, Joseph S, Holst MJ, McCammon JA (2001) Electrostatics of nanosystems: application to microtubules and the ribosome. Proc Natl Acad Sci U S A 98: 10037–10041.

59. O'Callaghan CA, Byford MF, Wyer JR, Willcox BE, Jakobsen BK, et al. (1999) BirA enzyme: production and application in the study of membrane receptor-ligand interactions by site-specific biotinylation. Anal Biochem 266: 9–15.